Sedimentation instability: A numerical and experimental study

Michael Niebling

Thesis submitted for the degree of Philosophiae Doctor

Faculty of Mathematics and Natural Sciences - Department of Physics
University of Oslo, Norway

September 2009

Series of dissertations submitted to the
Faculty of Mathematics and Natural Sciences, University of Oslo
No. 915

ISSN 1501-7710

Cover: Inger Sandved Anfinsen.
Printed in Norway: AiT e-dit AS, Oslo, 2009.

Produced in co-operation with Unipub AS.
The thesis is produced by Unipub AS merely in connection with the
thesis defence. Kindly direct all inquiries regarding the thesis to the copyright
holder or the unit which grants the doctorate.

Unipub AS is owned by
The University Foundation for Student Life (SiO)

Acknowledgments

Almost four years ago I was given the opportunity to write my Ph.D-thesis in the Advanced Materials and Complex Systems (AMCS) group at the University of Oslo. For this great experience I would like to thank my supervisor Professor Eirik Grude Flekkøy and co-supervisors Professor Knut Jørgen Måløy and Professor Renaud Toussaint for your support, helpful ideas and advice, and for introducing me to the exciting field of research on granular materials. Just as it was a privilege to be a student and work together with such experienced and inspiring scientists, on a personal level I enjoyed and feel grateful for the supportive atmosphere in the AMCS group. For this motivating spirit I also want to thank all members of the AMCS group my fellow students and friends.
I would like to thank the Norwegian Research Council and the Petromaks program for the funding of the project, and Professor Eirik Grude Flekkøy and Professor Knut Jørgen Måløy for extending my grant for the last months.
A special thanks goes to Joachim Mathiesen and Øistein Johnsen for proofreading.

Oslo, August 2009
Michael Niebling

Contents

List of Papers

Paper 1 Michael J. Niebling, Eirik G. Flekkøy, Knut Jørgen Måløy, and Renaud Toussaint: *Mixing of a granular layer falling through a fluid.*
Submitted to Physical Review E

Paper 2 Michael J. Niebling, Eirik G. Flekkøy, Knut Jørgen Måløy, and Renaud Toussaint: *Sedimentation instabilities: impact of the fluid compressibility and viscosity.*

1 Introduction

1.1 A granular world

Granular materials appear in various natural and processed forms. In example a total of 10% of the earth's land surface is covered by granular materials in form of sand in shore lines and desserts, as exemplified through the picture gallery in Fig. 1.1 [1]. Avalanches [2] and land slides [3], or the formation and migration of desserts can represent extreme threats to whole land areas and people and are typical phenomena of granular materials.

With a world wide production of nearly 10 billion metric tons every year of grains and aggregates an estimated 10% of the entire energy produced on earth is used for the transport and handling of granular materials [1, 4, 5]. In many of our industrial plants up to 50% of the capacity is wasted due to problems related to the transport of these materials. After water granular materials are the second most processed materials in the industry. Typical examples for industries that are handling granular materials on a daily basis are the pharmaceutical industry with the processing of powders and production of pills, the mining and construction industry, or agriculture and food industry.

Because of the omni-presence of granular materials the understanding of their behavior is of great importance, and gained knowledge has the potential to lead to improvements in a wide field of applications.

1.2 Research in granular materials

The early history of research in the field of granular materials dates back more than two centuries with the pioneering work of Charles de Coulomb who formulated the Coulomb friction law in 1773 [6]. Sixty years later Michael Faraday discovered the spontaneous formation of pattern in sand induced by vibrations, the Faraday heaping [7]. Around that time, Osborne Reynolds, already well known for his studies in the field of hydrodynamics, made some fundamental contributions to the theory of granular materials, i.e. the concept of dilatancy [8]. For a longer period little attention was dedicated to the research in the field of granular materials compared to i.e. hydrodynamics. It was not until the 1950s that granular materials attracted the interest of an increasing number of

(a) Sand dune (b) Snow avalanche (c) Quicksand (d) Liquefaction (e) Ice bergs

Figure 1.1: Examples of granular materials in some of their versatile forms: (a) Sand and air form dunes in the Namibian dessert, (b) a snow-avalanche in the Swiss Alps [9], sand saturated with water reduces the friction between the grains often referred to as quicksand (c) [10], (d) buildings collapsed on liquefied sand during earthquakes in Japan [11, 12] and drifting icebergs off the shore of Iceland (e) [13].

scientist.

Commonly a granular material is defined as a conglomeration of discrete particles. However, for being defined as a granular material, it is a necessary criterion that the size of the grains is large enough to ensure that quantum effects and thermal fluctuations such as Brownian motion are unimportant, and the particles only interact through contact forces. The particles size lies in the range of a few micro meters, or on the other extreme reach several meters. Examples of granular materials are powders, sand, rice, cereals, rock boulders, snow and even ice bergs as shown in the picture gallery in Fig. 1.1.

Despite the simple definition of granular materials its dynamics is highly complex. Until now there is no complete theory able to capture the full depth of this dynamics in a similar way as the Navier-Stokes equations in hydrodynamics. The dynamical behavior of granular materials is different from the behavior known from any other form of matter, and in this sense granular materials form an additional state of matter.

Even though under certain circumstances a granular medium can adopt characteristics of a solid, fluid, or a gas, there are still plenty of distinctions. For example do granular materials produce avalanches and expand under deformation, known also as dilatancy after Reynolds [8]. Both is not observed with classical fluids and solids. Solid-like behavior for example can be experienced by placing a rock on sand where the sand supports the weight of the rock, or by building a sand castle from wet sand. This picture of a solid material however only stands until the sand is exposed to vibrations causing the sand to liquefy and the rock to sink. On a larger scale vibrations released by earthquakes caused the collapse of buildings build on compacted sand, as shown in Fig. 1.1(d) [14, 15].

In the research field on granular materials it is distinguished between dry granular

materials in vacuum or when the interstitial fluid is negligible, and wet granular materials where the interstitial fluid has an effect on the granular system.

In the simplest case, experiments are performed with static grains that show macroscopic solid-like behavior and develop force chains under gravitation or an external stress (see Fig. 1.2(a)) [16–18]. Force chains are typical attributes of granular materials and unlike Hooke's law in classical solids. According to Hooke's law, the tensile stress in classical solids is homogeneous and proportional to the deformation of the solid. The stress inside the granular media however is concentrated along distinct chains of neighboring particles that extend over many grain diameters. Through such force chains a packing of grains can redirect much of the gravitational stress to the confining side walls. In example in a cylinder filled with a granular packing, the measured weight at the bottom of a cylinder can be much lower than the physical weight of the packing of grains due to the Coulomb friction between the side walls and the column of grains [6, 19].

One of the most prominent and interesting features of granular materials is the transition of solid-like behavior to fluid-like behavior. Over the last decades this transition has been studied intensively in sand pile experiments [20, 21]. The transition occurs when the slope of the sandpile reaches a critical angle similar to the critical point in a classical phase transition. At this critical slope, known as the angle of repose, grains on the surface of the pile suddenly start to flow as avalanches.

The dynamic fluid-like state of granular materials is reached when the kinetic energy of the system allows the individual grains to leave the compacted state. Kinetic energy may be added to a system through vibrations, gravitation forces, and in wet granular materials through a fluid. The fluid-like state shows an array of spectacular features such as liquefaction due to vibration, or separation of the particles by size. Particles of different sizes may separate under vibrations referred to as the Brazil nut effect [22–24]. Vibrations with a certain frequency cause the large particles to move to the top of a packing of beads while smaller particles accumulate in the bottom of the packing. Changing the frequency the Brazil nut effect can also be reversed. Separation of the particles by size may also be induced by a gravity driven flow known as stratification [25, 26].

Streams of grains accelerated by gravitation are known from hour glasses or granular jets in Fig. 1.2(b). Granular jets can emerge if a large heavy sphere is dropped into a loosely packed bed of fine particles. Right after the impact a focused jet of sand shoots upwards, very similar to when a drop of water falls on the fluid surface [27, 28]. Granular streams in free fall are shown to have a surface tension and break into droplets just like a fluid [29](see Fig. 1.2(d)).

In nature granular materials are generally coupled through a viscous drag to a fluid or gas. When the interstitial fluid affects the dynamic of the grains, the system can be considered as a two phase system. The interplay between the grains and the interstitial

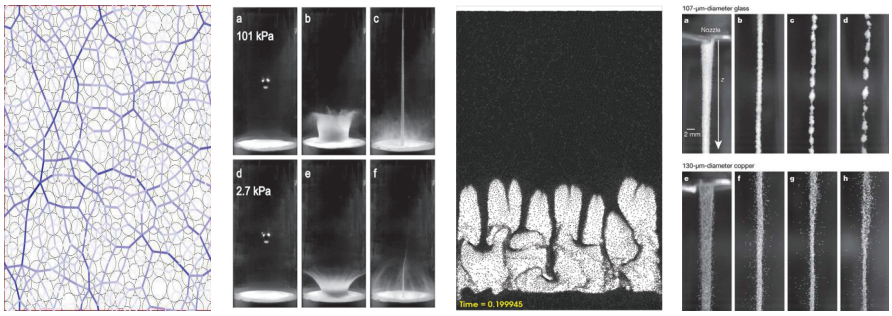

(a) Force Chains (b) Granular Jet (c) Granular Rayleigh Taylor instability (d) Granular stream

Figure 1.2: Research examples: (a) Forces chains in a simulation of static grains. The shading of the lines between particles illustrates the intensity of the inter-particle force. [40], (b) granular jets emerge after the impact of a heavy sphere into a bed of loose sand [27, 28], (c) interplay between air and grains: the granular Rayleigh-Taylor instability shows distinct fingers of high particle density and (d) a dry granular stream in free fall brakes up into droplets similar to a stream of water [29].

fluid results for example in sand dune migration and ripple formation [30–32], erosion [33], submarine landslides [34], and quicksand [35, 36].

The impact of an interstitial fluid in wet granular materials are studied in experiments where a granular material is fluidized by an injected fluid. Depending on the injection rate and the particle size the injected fluid may form bubbles of low particle density on the way through the granular material. Further examples of wet granular systems are the granular analog to the Saffman-Taylor [37–39], and the granular Rayleigh-Taylor instability that is studied in this thesis (shown in Fig. 1.2(c)).

1.2.1 Numerical methods in granular materials

The goal of numerical models is to start with a basic description of the discrete grains and predict the actual behavior of a real granular system and test theoretical hypotheses. The difficulty is, apart from providing the computer power needed to solve a system high number of particles, to capture and incorporate the essential micro-mechanical properties to describe the interactions between the grains. In general it can be distinguished between event driven integrators [41] and time stepping integrators of Newton's equations. The event driven model keeps track of the velocities and positions of all particles and the next collision can be predicted and accounted for before the procedure is repeated sequentially. Known methods to implement event driven models are contact dynamics [42, 43], Monte-Carlo [44, 45] and steepest decent [46] simulations. Time

stepping integrators solve Newton's equations by approximating in discreet time steps. Particle collisions can last several time steps, and more than one particle collision can occur during a time step. For systems with a high number of particles this technique is preferred. The time stepping algorithm is typically implemented with particle dynamics and hard spheres or molecular dynamics [47] with soft spheres. Particle dynamics treat the particles as hard spheres that do not deform or overlap under collisions. In molecular dynamics soft spheres do overlap and the magnitude of interaction depends on the penetration depth during particle collisions. Soft spheres collisions have a non zero duration in time in contrast to particle dynamics models. In this thesis we will implement the particles as soft spheres. A time stepping integrator with a molecular dynamics description and a velocity Verlet scheme for approximation is applied.

2 The granular Rayleigh-Taylor instability

In the classical case of the Rayleigh-Taylor instability a layer of a fluid with higher mass density is located on top of a fluid with lower mass density as shown in Fig 2.1. Due to gravitation the heavy fluid is accelerated into the lighter fluid and every infinitesimal small perturbation in the interface between the two fluids starts to grow. In this mixing process the system seeks to minimize its combined potential energy. As the instability develops the heavy fluid moves downwards in finger-like structures and displaces the lighter fluid that moves upwards in form of bubbles [48, 49].

In the laboratory the Rayleigh-Taylor instability is typically studied in Hele-Shaw cells. The natural equivalent occurs in systems with a very large difference in scale. An example on small scales is the violent collapse through a Rayleigh-Taylor instability of cavity bubbles if fluids [51, 52]. On the other side of the size scale are the mixing of sea water of different salinity [53], nuclear fusion reactions with magnetic [54], inertial [55] or gravitational confinement [56], nuclear weapons or supernova explosions [57, 58] and interstellar gas as in the crab nebula.

In the work presented in this thesis the heavier fluid is replaced by particles of higher mass density than the mass density of the interstitial fluid. This granular version of the Rayleigh-Taylor instability is studied by experiments and numerical simulations. There are some crucial differences between the system with two fluids and the granular Rayleigh-Taylor instability: The granular system lacks the surface tension of the granular phase and grains, and walls will interact with the grains through friction forces as known from the Janssen effect [19].

In general, the falling layer separates into three different zones, in the top and bottom part of the cell sit compacted particles that barely move and in the space between these two zones, we have a region of moving particles of lower particle density perturbed by the spontaneous formation of finger-like regions of higher particle density.

In contradistinction to previous works [59–64] where focus has been on the evolution of the interface between the moving particle-zone and the compacted particles at the top of the cell, we shall here analyze in detail the effect of the interstitial fluid on the mixing dynamics of the grains with the fluid and on the sedimentation of the grains. In

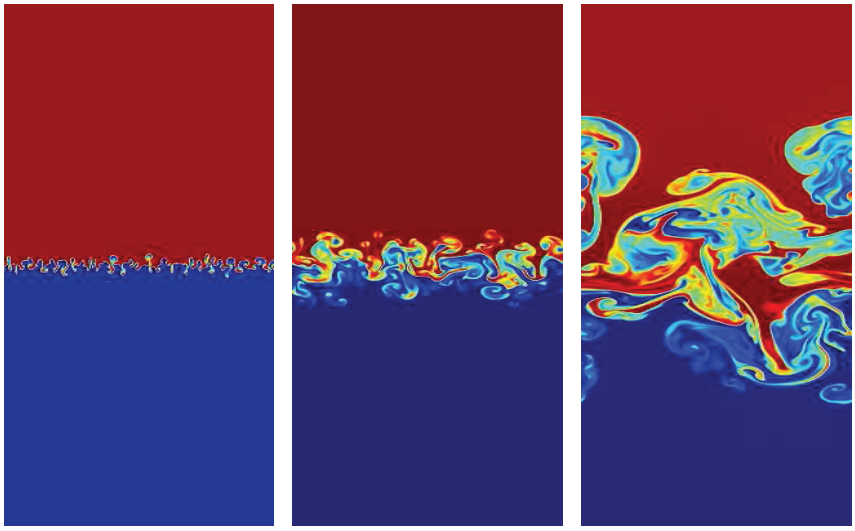

(a) (b) (c)

Figure 2.1: Simulation of the Rayleigh-Taylor instability in the classical case with two fluids of different mass density [50].

particular the effect of the fluid viscosity and fluid compressibility is analyzed.

3 Experiments

Experiments are carried out in a Hele-Shaw cell with air as an example for a compressible fluid and a water/glycerol solution as an incompressible fluid. Particles with different colors are used to improve the tracking of the particles and analyze the dynamics.

3.1 Experimental Setup

The Hele-Shaw cell used in the experiments consists of two rectangular glass plates with the inner dimensions w =5 cm in width by l =8 cm in height and a plate spacing of 1 mm as shown in Fig. 3.1. An adhesive 1 mm thick and 3 cm wide silicone frame holds the plates together and ensures the cell to be tight towards three sides. The particles are inserted through the open fourth side in small portions until the cell is filled to 3/4 with particles. Finally liquid silicone paste is applied all along the edge of the plates and also to the open fourth side to create a water or air-proof seal.

To better visualize the mixing a first series of experiments was performed with different colored particles deposited in layers at the beginning of the experiments. In a second series of experiments an amount of 10% of colored particles was randomly dispersed in the packing to act as tracers for the numerical extraction of the velocity by the CIV (Correlation image velocimetry) technique. The colored particles were of the same density as the uncolored particles in the case of air and in the case of water/glycerol. In the case of air Dynoseed polystyrene beads with a mass density of ρ_{m_p}=1.05 g/cm^3 and for water/glycerol glass beads with a mass density of ρ_{m_g}=2.5 g/cm^3 are used. In both cases we sieved particles with an average diameter of 140$\pm$10% μm. This corresponds to a number of 180000 particles in the simulations.

To assure reproducibility and to minimize the electro-static interaction and the cohesion between particles a relative humidity of 30% at 22° in temperature was maintained. For air the viscosity was $\mu_f(\mathrm{air})$ = 0.0182 mPa·s and the water/glycerol solution has a mass concentration of 30% glycerol, and the viscosity was measured to be $\mu_f(\mathrm{water/glycerol})$=0.00226 Pa·s with a mass density of ρ_f=1.065 g/cm^3.

After the preparation of the cell, confining the layered grains of different color, it is then carefully mounted on a rotating bar and fastened with clamps as shown in Fig. 3.1.

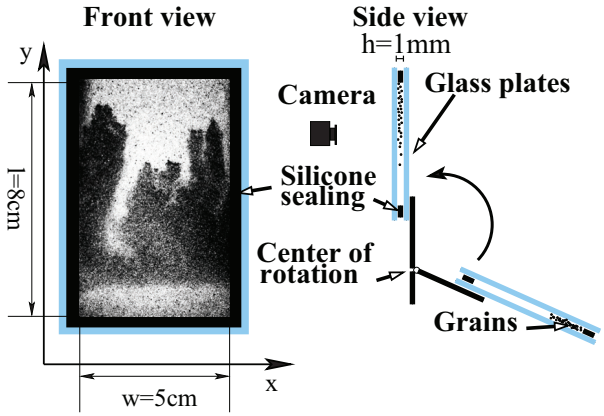

Figure 3.1: The experimental setup shown in front and side view: The Hele-Shaw cell consists of two rectangular glass plates with a spacing of 1mm. Silicone sealing assures the cell to be leak proof. The front view shows a picture taken during an experiment with water/glycerol.

In the second series of experiments, with randomly dispersed particles in the beginning the cell is flipped a couple of times in order to obtain an even surface and a random well mixed loose packing of particles at the beginning of the experiments. The positioning of the grains above the air or the water/glycerol solution is done by rapidly rotating the cell manually, until it reaches a vertical position. The center of rotation is located at the empty side of the cell. This generates centrifugal forces during the rotation that help to slow down the falling of the particles. The rotation is stopped by a stopping bar that is softened with a piece of expending rubber. Despite the damping of the cell, the initial patterns are perturbated by the impact. In the analysis, we therefore disregard the early stage of the experiments. During the experiments, pictures are taken by a high speed digital camera (Photron Fastcam-APX 120K) with a resolution of 512x1024 pixels. In the case of air pictures are taken at a rate of 1000 fps (frames per second) and in the case of water/glycerol where the dynamics are slower at a rate of 50 fps.

3.1.1 Experimental Picture Analysis

To compare the velocity field of the particles in the experiments to the simulations, a correlation image velocimetry (CIV) technique [65] is used. The images have 255 gray-levels and a resolution of 512x1024 pixels. The CIV technique allows to determine the displacement dx, dy of squared zones of size $(2i+1)^2$ pixels centered at x, y between two successive images as shown in Fig. 3.2. According to classical techniques [66] the displacement is calculated by the maximization of the cross-correlation of the gray-

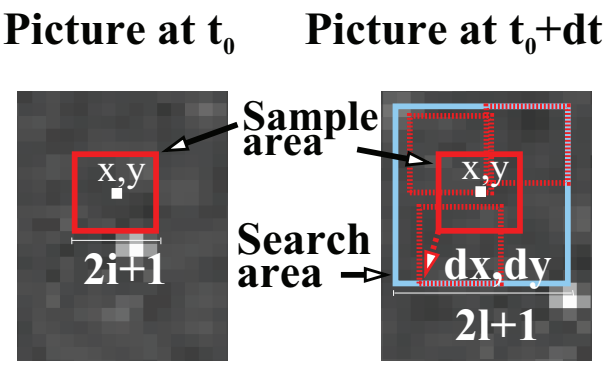

Figure 3.2: The correlation image velocimetry (CIV) technique: The gray-level cross correlation of two pictures in a time sequence is maximization for different displacements of the red a sample area within the search area shown in blue.

map of squared zones centered at x, y in the first image, and $x + dx$, $y + dy$ in the second one. To apply this technique the time resolution between two pictures must be good enough that the gray-map of the zones does not change significantly between two pictures. In addition to the classical treatment, we have developed an additional filtering method for the resulting velocity field, utilizing the fact that the obtained maximum cross-correlation is a measure of the resemblance between the zones, and thus of the suitability of the CIV technique for the zone under consideration.

To minimize the impact of artifacts due to aberrant zones where no resemblance is found with the subsequent pictures, we convolve the velocity field obtained by a weight, that increases the better the cross-correlation between the zones is. More specifically, for zones of interest of the size $2i + 1$ centered at x_0, y_0 and x_1, y_1, the cross-correlation between gray-map A and B is defined as:

$$\langle A(x_0, y_0)B(x_1, y_1)\rangle_i \equiv \sum_{m=-i}^{i}\sum_{n=-i}^{i} A(x_0 + m, y_0 + n)B(x_1 + m, y_1 + n) \tag{3.1}$$

and

$$\langle A(x_0, y_0)\rangle_i \equiv \sum_{m=-i}^{i}\sum_{n=-i}^{i} A(x_0 + m, y_0 + n). \tag{3.2}$$

For $s_1(x, y)$ and $s_2(x, y)$ the two gray-maps of two successive images, the normalized

gray-maps are defined as:

$$s_1'(x,y) = s_1(x,y)/\sqrt{\langle s_1(x,y)s_1(x,y)\rangle_i}$$
$$s_2'(x,y) = s_2(x,y)/\sqrt{\langle s_2(x,y)s_2(x,y)\rangle_i}, \tag{3.3}$$

and the cross-correlation between the two pictures as:

$$C(x,y,\Delta x,\Delta y) = \langle s_1'(x,y)s_2'(x+\Delta x, y+\Delta y)\rangle_i. \tag{3.4}$$

The displacement $dx(x,y), dy(x,y)$ between two successive pictures for zones centered on (x,y) is determined from maximizing $C(x,y,\Delta x,\Delta y)$ over $\Delta x, \Delta y$, i.e. such that:

$$C(x,y,dx,dy) = \max_{\Delta x,\Delta y \le l}[C(x,y,\Delta x,\Delta y)] = C_{max}(x,y). \tag{3.5}$$

For this maximization, search values of $l = 6$ pixels maximum displacement for Δx, Δy, and sample squares of 7x7 with $i = 3$ pixels are used. Next, the resulting displacement is convolved on running square windows of linear size l, with a weight $w(x,y) = 1/(3 - 2C_{max}(x,y))$ on each pixel, i.e. we determine a final average displacement

$$dx_{fa}(x,y) = \frac{\langle w(x,y)dx(x,y)\rangle_i}{\langle w(x,y)\rangle_i} \tag{3.6}$$

$$dy_{fa}(x,y) = \frac{\langle w(x,y)dy(x,y)\rangle_i}{\langle w(x,y)\rangle_i} \tag{3.7}$$

The resulting procedure is tested on simulated images, by comparing directly the resulting determined velocity field with the one calculated for the particles in the corresponding simulation.

The resulting procedure is tested and illustrated in Fig. 3.3. The displacement field is shown in white arrows in pictures from the experiments with air Fig. 3.3(a) and with water/glycerol Fig. 3.3(b). An additional test comparing the velocity field of the simulations with the velocity field determined by the CIV technique from pictures of this simulations revealed that the average angle between the vectors of the two velocity fields was $\alpha = \langle |\arccos[(\mathbf{u_{civ}} \cdot \mathbf{u_{sim}})/(u_{civ}\, u_{sim})]|\rangle = 6.07°$. Restricted to areas where particles travel in distance 0.9 and 3.2 of their diameter between two pictures.

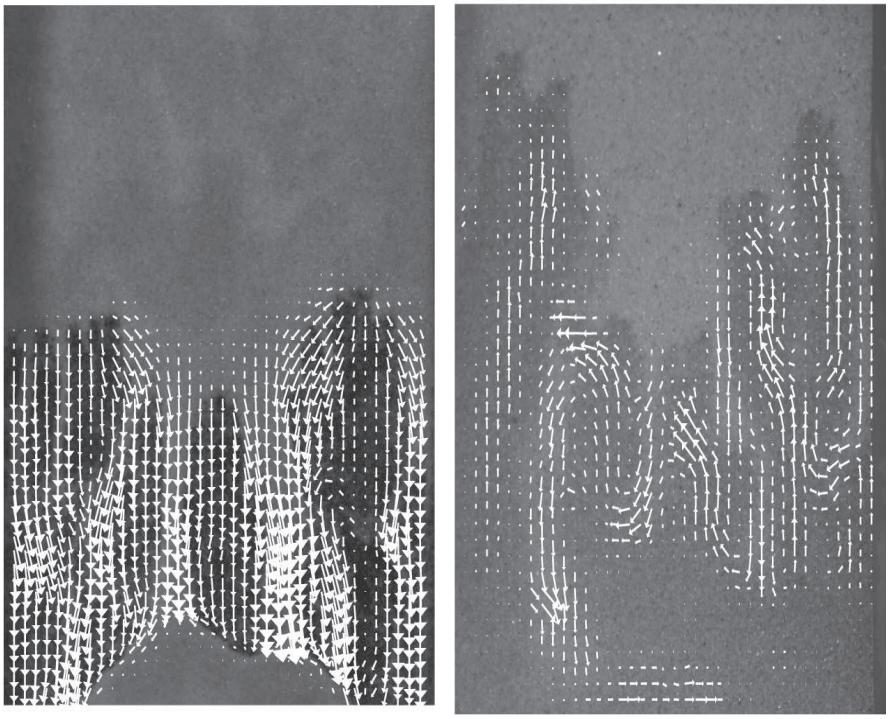

(a) (b)

Figure 3.3: The velocity field visualized with white arrows in experiments with air (a) and with water/glycerol (b) extracted with the CIV technique.

4 Theory and Simulations

The numerical simulations have to deal with a coupled two phase system consisting of solid grains with an interstitial fluid. The model reflects the natural features of the two phases by employing a discrete description for the particles, and a continuum description for the fluid part. The granular phase assembles to a deformable porous media and interacts with the ambient fluid through the granular velocity $\mathbf{u}$ and the local permeability κ. Using mass conservation and Darcy's law, the non-hydrostatic part of the pressure P, the hydraulic head, can be calculated for each particle constellation. P corresponds to $P = P' - \rho_f g y'$, where P' is the pressure, g the gravity constant, ρ_f the mass density of the fluid and y' the depth. The hydraulic head then contributes to the net force on a volume element dV which is balanced by the acceleration of the grains and the fluid in this element according to Newton's second law.

In this work molecular dynamics and a velocity Verlet scheme is used to simulate the particles, however, contact dynamics can also be applied [63]. When the model was developed in the studies [39, 63, 67–69]. It was designed to capture the macroscopic behavior of the system rather than the dynamics of single particles in order to keep the model computationally affordable. Therefore, the hydraulic head and the local solid volume fraction ρ_s is discretised on a square grid of 2.5 times the particle diameter.

4.1 Dynamics of the fluid - conservation of mass

A general form of the pressure equation is derived from mass conservation of the fluid and mass conservation of the particles and the fluid velocity is linked to the Pressure gradient by Darcy's law [68, 69]. To include the compressibility of the fluid β_T the fluid mass density is approximated to be proportional to the pressure. The hydraulic head is calculated by solving the following diffusion equation:

$$\phi \left[\frac{\partial P}{\partial t} + \mathbf{u} \cdot \nabla P \right] = \nabla \cdot \left[\hat{P}(\beta_T) \frac{\kappa}{\mu} \nabla P \right] - \hat{P}(\beta_T) \nabla \cdot \mathbf{u}. \tag{4.1}$$

$\hat{P}(\beta_T) = P - P_0 + 1/\beta_T$ and $\beta_T = 1/\kappa_T = -\frac{1}{V}\frac{\partial V}{\partial P}$ the fluid compressibility where κ_T is the bulk modulus and P_0 the background pressure. $\phi = 1 - \rho_s$ is the porosity,

μ the viscosity of the fluid and κ the local permeability. In Eq. (4.1) the pressure at a given position changes in time when the pressure field moves with the grains according to the velocity of the grains: $\mathbf{u} \cdot \nabla P$. On the right hand side the first term accounts for pressure changes due to fluid motion relative to the particles. The second term is a source/sink term that accounts for the pressure change due to the change of solid filled volume. If particles move together the pressure increases or apart from each other the pressure drops.

In the case of air as an ideal gas $\beta_T = 1/P_0$ at P_0 and Eq. (4.1) results in:

$$\phi \left[\frac{\partial P}{\partial t} + \mathbf{u} \cdot \nabla P \right] = \nabla \cdot \left(P \frac{\kappa}{\mu} \nabla P \right) - P \nabla \cdot \mathbf{u}. \tag{4.2}$$

In the incompressible limit when $\beta_T \to 0$ Eq. (4.1) results in a Poisson equation

$$\nabla \cdot \left(\frac{\kappa}{\mu} \nabla P \right) = \nabla \cdot \mathbf{u}. \tag{4.3}$$

This equation simply states mass balance between solid and liquid volume. The displaced fluid volume is replaced by volume of grains. In both cases we calculate the local permeability κ by the Carman-Kozeny relation:

$$\kappa = \frac{a^2}{9K} \frac{(1-\rho_s)^3}{\rho_s^2} \tag{4.4}$$

with $\rho_s = 1 - \phi$ the solid volume fraction, a the particle radius and $K = 5$ an empirical constant valid for a packing of spherical beads [70].

4.2 Dynamics of the particles - Newton's second law

The acceleration of a unit volume dV filled with a total particle mass of $\rho_m \rho_s dV$, with a particle mass density of ρ_m, and the total fluid mass of $\rho_f \phi dV$ is equal to the net stress integrated over it's surface dA as shown in Fig. 4.1.

$$\begin{aligned} \rho_m \rho_s dV \frac{d\mathbf{u}}{dt} \quad &+ \quad \rho_f \phi dV \frac{d\mathbf{v_f}}{dt} = \rho_{eff} \rho_s dV \mathbf{g} + \\ \sum \mathbf{F_I} \quad &- \quad \int P \mathbf{dA} + \int \sigma_t dA + \mathbf{F}_\gamma. \end{aligned} \tag{4.5}$$

$\mathbf{F_I}$ refers to the inter-particle contact force, σ_t is the tangential stress between the fluid flow and the confining plates, and $\mathbf{g}$ the acceleration of the gravitation. $\mathbf{F}_\gamma$ accounts for the energy dissipation during particle collisions, and the friction forces between the particles and the confining plates (see section 4.2.1). The effective mass density is

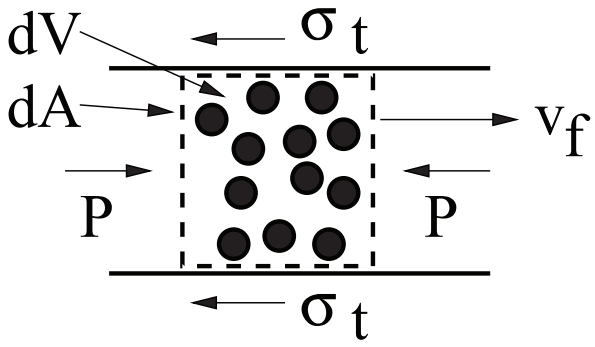

Figure 4.1: Stress and pressure acting on the surface dA of a unit volume dV.

$\rho_{eff} = \rho_m - \rho_f$. The friction between the fluid and the walls due to the tangential stress σ_t is proportional to the fluid velocity and plays an essential role only in the dynamic zone of the Hele-Shaw cell where particles are dispersed and effectively moving.

This equation (4.5) can be simplified if the mass density of the fluid is low compared to the mass density of the grains, as for i.e. air and glass beads. In this case the second term on the left hand side in Eq. (4.5), the inertia of the fluid can be neglected. If the fluid viscosity is high and the mass density of the grains close to the mass density of the fluid in Eq. (4.5) the acceleration of the fluid can be approximated by the acceleration of the particles:

$$\frac{d\mathbf{u}}{dt} \approx \frac{d\mathbf{v_f}}{dt} \tag{4.6}$$

and Eq. (4.5) results in:

$$\begin{aligned} [\rho_m \rho_s dV + \rho_f \phi V] \frac{d\mathbf{u}}{dt} &= \rho_{eff} \rho_s dV \mathbf{g} + \sum \mathbf{F_I} - \\ \int \nabla P dV + \int \sigma_t dA &+ \mathbf{F}_\gamma. \end{aligned} \tag{4.7}$$

This approximation was validated and used in the first article of this thesis (*Mixing of a granular layer falling through a fluid.*) and allows to incorporate fluid inertia of a stream consistent of several particles and the surrounding fluid. The approximation does not account for the fluid inertia associated with the relative fluid flow to the particles, and does not change the drag force from the fluid on the particles.

Each individual particle has a mass of $m = \rho_m \pi a^2 h$, volume $V_a = \pi a^2 h$, and base area $S_a = \pi a^2$ where h is the plate spacing. To access the acceleration of the individual particle the unit volume in Eq. (4.7) is set to be $dV = 1/\rho_n$ with the number density

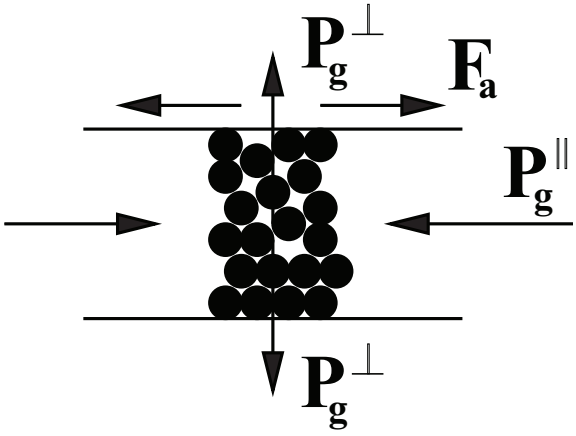

Figure 4.2: The Janssen effect: The in-plane $P_g^{||}$ stress is being deflected by the particles resulting in a normal stress $P_g^{\perp}$ on the plates.

$\rho_n = \rho_s \rho_m / m$ resulting in:

$$\left[m + \rho_f \frac{\phi}{\rho_n} \right] \frac{dv_p}{dt} = \rho_{eff} V_a \mathbf{g} + \mathbf{F_I} - \frac{\nabla P}{\rho_n} + \frac{\sigma_t S_a}{\rho_s} + \mathbf{F}_{\gamma_\mathbf{p}}. \tag{4.8}$$

This is the force equation for each single particle with the velocity v_p. The mass of the fluid appears in the first term of this equation and is simply added to the mass of a particle. The amount of mass from the fluid that we add to the mass of each particle depends on the local porosity divided by the number density. This allows to incorporate the fluid inertia to the model by changing the particle mass into a "fluid-coated" particle mass.

The inter-particle force $\mathbf{F_I}$ is set to be a linear force with a spring constant strong enough that the particles only overlap a negligible fraction of their diameters.

4.2.1 Solid friction forces

Friction between the side plates and the grains is playing a significant role in the experiments. Apart from the friction between the fluid and the plates that is included in Eq. (4.7) through σ_t, friction also occurs directly between the side walls and the particles. In contrast to the friction between the fluid and the plates which is negligible in the top and the bottom of the Hele-Shaw cell due to the low velocity of the fluid. The friction mechanism between the side walls and the particles is primarily active in the top and the

bottom of the Hele-Shaw cell where particles are compacted and hardly moving. In the situation of compacted particles the compressive in plane stress $P_g^{||}$ generates a proportional normal stress on the plates according to the Janssen hypothesis [19]. λ is defined as the proportionality constant between the normal and the in-plane stress. A Coulomb friction model with a friction coefficient γ gives the friction force for each particle:

$$F_a \leq 2\gamma S_a P_g^{\perp} = 2\gamma\lambda S_a P_g^{||}. \tag{4.9}$$

Friction forces between particles are neglected. However, energy dissipation is included with a restitution coefficient of r =0.55. In the molecular dynamics model the energy dissipation is introduced through a viscous force between two colliding particles through:

$$\mathbf{F_d} = -\gamma_d(\mathbf{v_r}\cdot\mathbf{n_d})\mathbf{n_d}. \tag{4.10}$$

The magnitude of this viscous force is proportional to the relative velocity $\mathbf{v_r}$ of the particle pair projected on the unit vector $\mathbf{n_d}$, which points from the center of one particle to the contact point. The direction of this force is given by the opposite direction of the unit vector $\mathbf{n_d}$. The friction force F_a in Eq. (4.9) and the viscous force $\mathbf{F_d}$ in Eq. (4.10) enter as $\mathbf{F}_\gamma$ in Eq. (4.7).

4.3 Implementation

In the model the solution algorithm of the pressure equation operates on a square lattice with a lattice constant of $l = 2.5$ times the average particle diameters. To define the solid volume fraction ρ_s, and the granular velocity $\mathbf{u}$ at each of this lattice nodes, a halo function is used to average over the particles at position $\mathbf{r} = (x, y)$ between the node at $\mathbf{r}_0 = (x_0, y_0)$ and the next neighboring nodes. This halo function is defined as:

$$s(\mathbf{r}-\mathbf{r}_0) = \begin{cases} \left(1-\dfrac{|x-x_0|}{l}\right)\left(1-\dfrac{|y-y_0|}{l}\right) & \text{if } |x-x_0|, |y-y_0| < l \\ 0 & \text{otherwise}. \end{cases} \tag{4.11}$$

In this average the contribution of the particle at position $\mathbf{r} = (x, y)$ to the node at position $\mathbf{r}_0 = (x_0, y_0)$ is proportional to $s(\mathbf{r} - \mathbf{r}_0)$, and is larger in magnitude the closer the position of the particle x, y is to the position of the node at $\mathbf{r}_0 = (x_0, y_0)$. A graphical demonstration of the contribution is given in Fig. 4.3. The particle at position $\mathbf{r} = (x, y)$ contributes to the node at position $\mathbf{r}_0 = (x_0, y_0)$ according to the striped area in the picture. The halo function is used to smoothen the particle input into Eq. (4.2 and 4.3), and it serves as well to distribute the pressure from the nodes to the individual particles.

On the square grid the pressure equation is solved in the case of a compressible fluid and the diffusion equation (4.2) with a Crank Nicholson scheme [71]. The Poisson

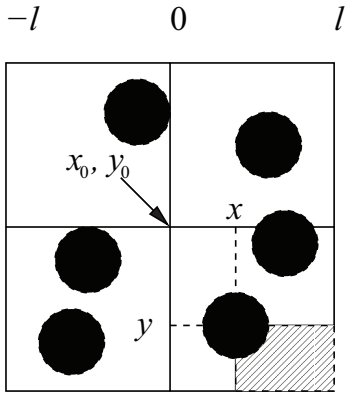

Figure 4.3: The halo function: A particle at position x, y contributes to the average over all particles at the node at position $\mathbf{r}_0 = (x_0, y_0)$ according to the striped area.

equation (4.3) for incompressible fluids is solved with a multi-grid integration scheme as presented in [71].

The particle dynamics follow Newton's second law as stated in Eq. (4.8). With the velocity Verlet method Eq. (4.8) is integrated for discrete time steps and the position, velocity and acceleration for each particle and the next time step are calculated in the following way:

$$\begin{aligned}
\mathbf{r_p}(t+\Delta t) &= \mathbf{r_p}(t) + \mathbf{v_p}(t)\Delta t + \frac{1}{2}\mathbf{a_p}(t)\Delta t^2 \\
\mathbf{v_p}(t+\frac{\Delta t}{2}) &= \mathbf{v_p}(t) + \frac{1}{2}\mathbf{a_p}(t)\Delta t \\
\mathbf{a_p}(t+\Delta t) &= \frac{1}{\left[m + \rho_f \frac{\phi}{\rho_n}\right]}\mathbf{F_{s_p}}\left(\mathbf{r_p}(t+\Delta t)\right) \\
\mathbf{v_p}(t+\Delta t) &= \mathbf{v_p}(t+\Delta t/2) + \frac{1}{2}\mathbf{a_p}(t+\Delta t)\Delta t. \qquad (4.12)
\end{aligned}$$

With r_p as the position and a_p the acceleration of a particle with index p, t as the time, Δt as the time step and $\mathbf{F_{s_p}}$ the sum of all forces acting on a particle. This method has the advantage that the local error is $\mathrm{error(x(t_0 + \Delta t))} = \mathcal{O}\mathrm{t}^4$ although only the second order terms are used.

To represent the 3d (dimensional) close packed solid fraction of the experiments in the simulation we multiply the 2d solid fraction in the simulations by a factor of 2/3, which is the solid fraction ratio between a randomly close packing of spheres to a randomly close packing of cylinders. To avoid singularities and because the Carman-

Kozeny relation is not valid below solid fractions of $\rho_s < 0.15$ in Eq. (4.4) $\rho_{s_{\min}} = 0.15$ is used as a lower cutoff.

5 Results

In the first part of this chapter the simulations with incompressible water/glycerol and compressible air are compared with well matched experiments to validate the numerical model. The dynamics and the sedimentation depend strongly on the interstitial fluid and the results are presented in the first article of this thesis (*Mixing of a granular layer falling through a fluid.*).

In a second part of this chapter the second article (*Sedimentation instabilities: impact of the fluid compressibility and viscosity.*) is summarized. An idealized numerical system, where the friction between the confining plates and the particles is neglected, is studied to identify the mechanisms causing the differences between the incompressible and the compressible case.

5.1 Comparison between experiments and simulations

In Fig. 5.1 simulations and corresponding experiments with air as the interstitial fluid are shown in the two upper time sequences, and with water/glycerol are shown in the two lower time sequences. Simulations and experiments show excellent agreement. The dynamics with particles immersed in compressible air show the evolution of downward falling fingers of high particle density between upwards moving bubbles of low particle density. The contrast in particle density between the bubbles is much higher compared to the particles emerged in water/glycerol where the density contrast between bubbles and fingers appears less pronounced. In the latter case the fingers are thinner and often disperse before they reach the bottom of the cell.

To demonstrate the different dynamics, particles of different colors are arranged in horizontal layers at the beginning of the experiments. In air the particles have settled (shown in Fig. 5.2) in cusp shape patterns in water/glycerol however a complete mixing is observed. In the simulation with water/glycerol in picture 5.2(h) two unmixed zones appear at the end of the simulations. This is not observed in the experiments with horizontal layers of different colored particles. Most likely this is due to the fact that after the Hele-Shaw cell was filled it was mounted on the rotating bar and exposed to additional stress from the clamps. The additional stress compressed the silicone sealing of the cell compacting the particles slightly which increased the friction with the side

walls. This only effects the first experiment in a row.

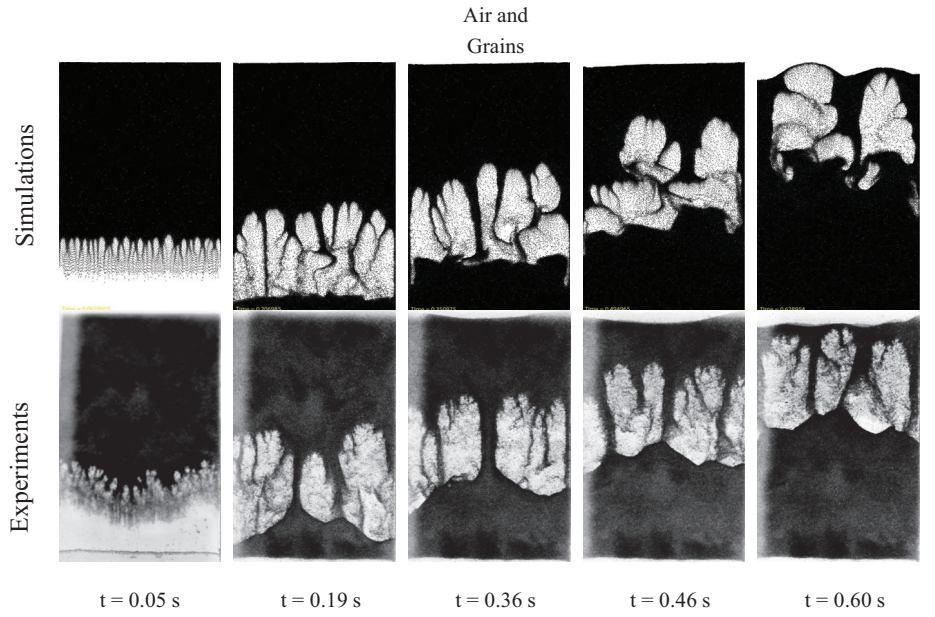

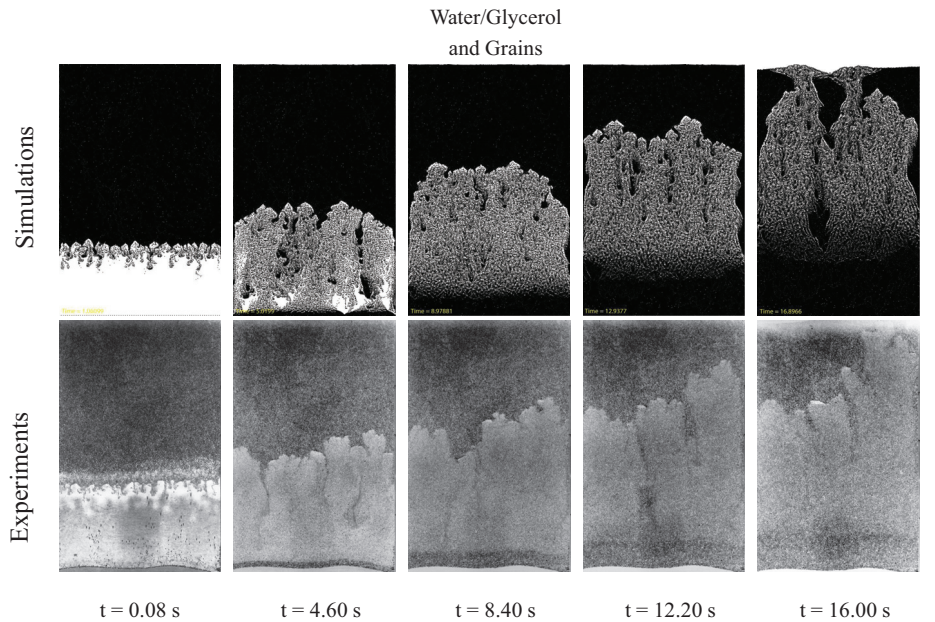

Figure 5.1: Simulation in comparison to experiments of the granular Rayleigh-Taylor instability with a particle diameter of 140 µm. The first sequence shows simulations and the second sequence shows corresponding experiments with air. In the third sequence simulations and the forth sequence corresponding experiments with water/glycerol are shown.

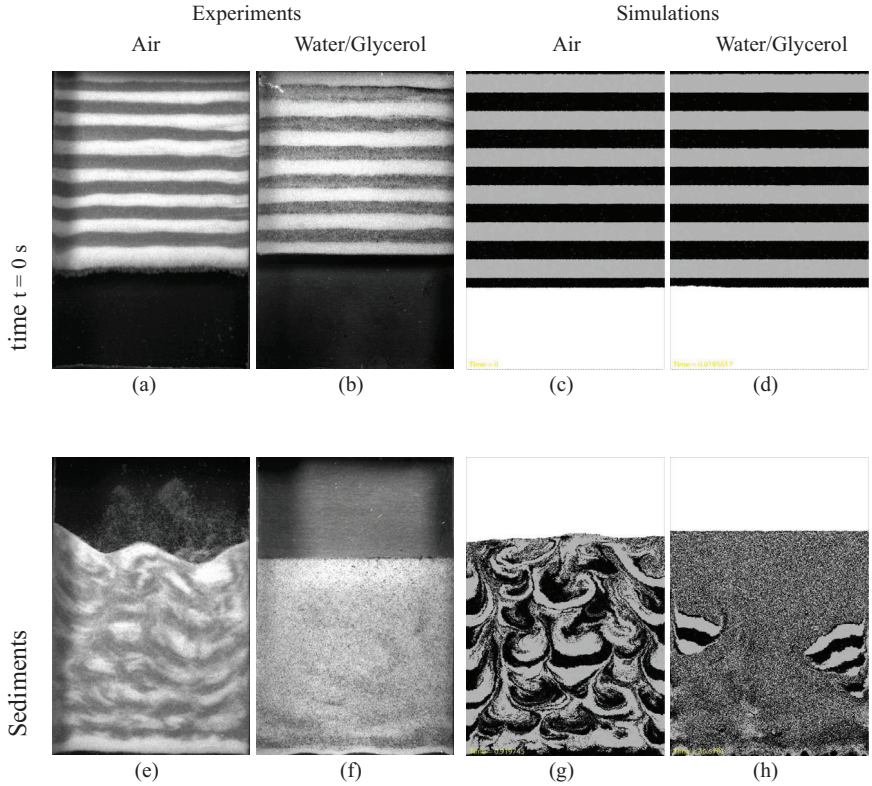

Figure 5.2: Experiments and simulations show cusp shape sedimentation patterns for grains and air. With grains and water/glycerol a complete mixing is observed.

6 Analysis

In this work velocity field histograms, wave numbers of the density- and velocity fields, and 2d velocity autocorrelation functions are used to verify the agreement between the experiments and the simulations. All these methods demonstrate a very good agreement, and in addition they enable to quantitatively distinguish the different mixing behaviors in the compressible and incompressible case.

6.1 2d Autocorrelations

The 2d velocity autocorrelation function is normalized by the standard deviation $C_\alpha(\mathbf{d})$ where $\alpha = x$, or y the x, or y- component of the velocity field $\mathbf{u}(i, j)$ is defined as:

$$C_\alpha(\mathbf{d}) = \frac{\sum_{\mathbf{r}}((u_\alpha(\mathbf{r}) - \langle u_\alpha \rangle)(u_\alpha(\mathbf{r}+\mathbf{d}) - \langle u_\alpha \rangle))}{\sum_{\mathbf{r}}(u_\alpha(\mathbf{r}) - \langle u_\alpha \rangle)^2}. \tag{6.1}$$

In Fig. 6.1 the velocity autocorrelation in 2d is shown for simulations and experiments with air in plot (a) and (b), and for simulations and experiments with water/glycerol in plot (c) and (d). The experiments show good agreement with the simulations in both cases, and time progresses from left to right in equal steps corresponding to the steps in Fig. 5.1. In Fig. 6.1 the top rows show the 2d autocorrelation of the u_x component of the velocity field, and the second row the u_y component of the velocity field. The autocorrelation of the u_x component of the velocity field shows equal distribution along the x- and the y-axis. The correlation is stronger when particles are immersed in air than in water/glycerol. The autocorrelation of the u_y component however shows periodic vertical lines of stronger correlation directed along the y-axis. The lines are thinner in the case of water/glycerol than with air. The frequency of the lines decreases with the progress of the experiments which reflects the coarsening process of the evolving structures. The less strong autocorrelation of the velocity field with air also indicates the better mixing of the settled particle after the experiments.

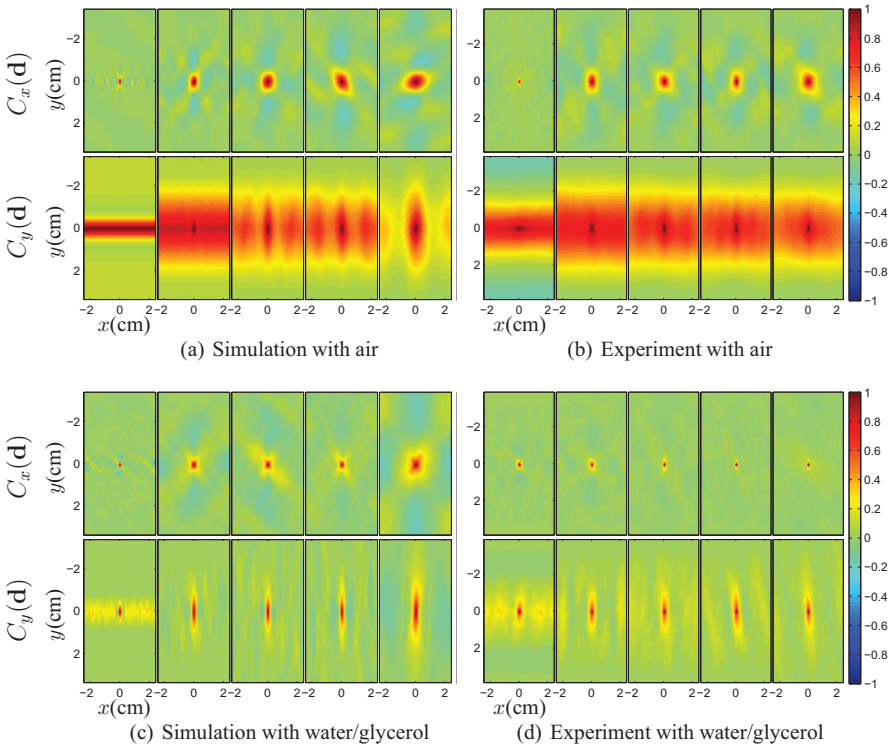

(a) Simulation with air (b) Experiment with air

(c) Simulation with water/glycerol (d) Experiment with water/glycerol

Figure 6.1: In the first rows a time sequence of the normalized autocorrelation of the x component of the velocity field $C_x(\mathbf{d})$ is shown with $\mathbf{d} = \binom{x}{y}$. The second rows show a time sequence of the normalized autocorrelation of the y component of the velocity field $C_y(\mathbf{d})$. In figure (a) and (b) simulations and experiments with grains and air are presented. Simulations and experiments with grains and water/glycerol are shown in the figures (c) and (d). The time steps from left to right correspond to Fig. 5.1.

6.2 Effects of the fluid viscosity and fluid compressibility

After the numerical simulations are tested and shown to be realistic the open question is, what causes the difference between the dynamics with air and water/glycerol. For this reason the effect of the fluid compressibility and the fluid viscosity on the dynamics shall be studied. The numerical model provides a valuable tool to answer this question since the simulations allow to vary the fluid compressibility and the fluid viscosity inde-

pendently. For this purpose a idealized numerical system is studied, where the friction with the side-walls and the fluid mass is neglected.

In Fig.6.2 the bulk modulus is varied from $\kappa_T = 1\,\mathrm{kPa}$ to incompressible behavior $\kappa_T = \infty$ at a fluid viscosity corresponding to air $\mu_f(\mathrm{air})$ =0.0182 mPa·s at room conditions of 25° C and atmospheric pressure. For $\kappa_T = 100\,\mathrm{kPa}$ and $\kappa_T = \infty$ the time sequence shows a similar structure of the fingers. However for a bulk modulus $\kappa_T = 1\,\mathrm{kPa}$ and time $t \leq 0.126\,\mathrm{s}$ bubbles of low particle density occur in the packing of grains in the top of the cell. The fluid in the empty bottom part of the cell also is compacted noticeably until the fluid supports the weight of the particle layer.

The effect of the fluid viscosity is shown in Fig. 6.3, where the viscosity is changed to $\mu_f(\mathrm{air})$ =0.678 mPa·s while the fluid is considered incompressible. The structure of the fingers for the increased viscosity is significantly different from the structures observed in Fig. 6.2. For a higher viscosity the fingers appear less straight and even disperse before reaching the bottom of the cell. Changing the fluid viscosity appears to affect the dynamics of the fingers much stronger than the fluid compressibility.

To answer the question if the compressibility of the fluid affects the mixing in a way

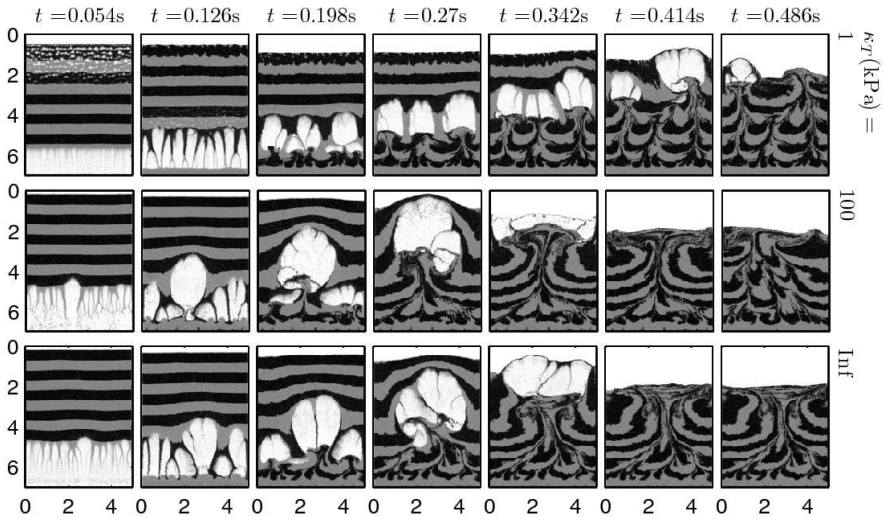

Figure 6.2: The effect of fluid compressibility at a fixed fluid viscosity of air: $\mu_f(\mathrm{air})$ =0.0182 mPa·s. Gray and black areas represent areas filled with particles. The stripes are added artificially to better demonstrate the dynamics. From left to right, time progresses in equal time steps, and from top to bottom the bulk modulus is increased.

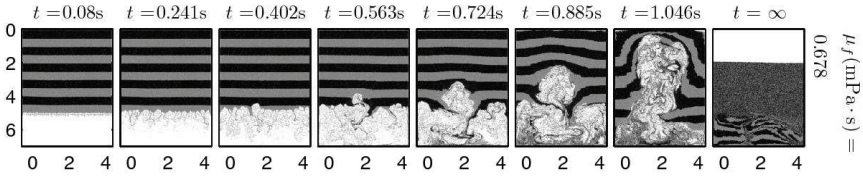

Figure 6.3: The density field of simulations in time. The viscosity is increased to the sequence in Fig.6.2 while the fluid is considered incompressible. If not specified the axis units are given in centimeters. White areas represent particle free areas.

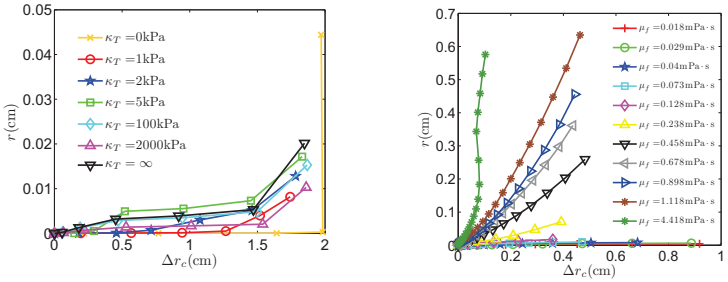

(a) (b)

Figure 6.4: The excess path length r in order of the center of mass Δr_c. In Fig. (a) for different fluid bulk moduli and in Fig. (b) for different fluid viscosity.

that could explain the differences observed between water/glycerol and air, the excess path length of the 8000 lowest the particles at $t = 0\,\mathrm{s}$ is calculated and shown in Fig. 6.4(a). The center of mass of this layer is $\Delta r_c(t) = r_c(t) - r_c(0)$ and the excess path length $r(t)$ is defined as:

$$r(t_s) = \frac{\sum_i^N \sum_{j=1}^s |\mathbf{r}_i(t_j) - \mathbf{r}_i(t_{j-1})|}{N} - (r_c(t_s) - r_c(0)), \tag{6.2}$$

where the position of the i-th particle is given by $\mathbf{r}_i(t)$ and the particle number $N = 8000$.

The plots of the excess path length show little difference if the compressibility is varied, and for all bulk moduli the particles fall almost straight through the gap of air with an excess path length of almost zero before the particles collide with the bottom of the cell at $\Delta r_c = 1.5\,\mathrm{cm}$. This shows that the compressibility is not the cause for the different mixing behaviors. However, if the interstitial fluid is taken to be incompressible, and the fluid viscosity is varied as shown in Fig. 6.4(b) for viscosities of $\mu_f = 0.018\,\mathrm{Pa{\cdot}s}$ to

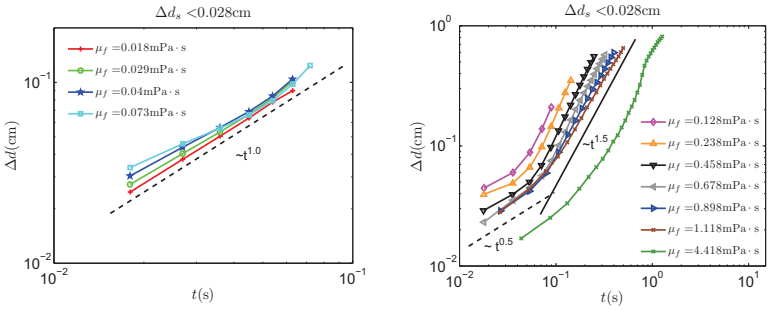

Figure 6.5: Δd the average distance of particle pairs in time for low (a) and high (b) viscous fluids in bilogarithmic representation. In (a) the power law fit with an exponent $b = 1.0$ shows ballistic behavior. In (b) the initial separation of the pairs has a diffusive behavior with an exponent close to $b = 0.5$ in the dashed line. In the progress a crossover to a turbulent-dispersive behavior is observed with a slope close to $b = 1.5$ in the solid line.

$\mu_f = 4.418$ Pa·s the plots of the excess path length changes significantly. In Fig. 6.4(b) the excess path length, in relation to the center of mass, increases the more viscous the fluid is.

These results show that the different mixing behavior in order of the interstitial fluid depends strongly on the viscosity of the interstitial fluid while the compressibility has a less critical influence on the system size studied. Numerically it is a big advantage if the compressibility can be neglected in terms of computational speed. In the presented simulations computation time can be up to 20 times smaller if the compressibility is negligible.

To further analyze the mixing Δd is defined as the average relative distance of particles pairs. At time $t = 0$ s these pairs where separated by a distance $\Delta d_s < 0.028$ cm, which corresponds to 2 particle diameters. To focus on the initial dynamics the average is taken only over the first 600 particles which corresponds to the first two particle layers. These two layers have the advantage to almost start moving instantaneously independent of the fluid viscosity. To avoid boundary effects the analysis is stopped when the first particle has reached a distance of 10 particle diameters to the lower boundary. In the bilogarithmic Figs. 6.5(a) and 6.5(b) the growth of Δd is shown and can be classified into two regimes. In Fig. 6.5(a) for low viscous fluids with $0.018\text{kPa} \cdot \text{s} \leq \mu_f \leq 0.073$ kPa·s the pair separation grows with a constant velocity between the particle pairs in a ballistic way and an exponent close to $b = 1.0$ in a power law fit of $\Delta d = at^b$. In Fig. 6.5(b) the second regime for high viscous fluids with $0.128\text{kPa} \cdot \text{s} \leq \mu_f \leq 4.418$ kPa·s shows a initial diffusive particle separation with an

exponent close to $b = 0.5$. In the progress a crossover to a turbulent-dispersive behavior with an exponent close to $b = 1.5$ can be observed. This exponent corresponds to the Richardson law that predicts an exponent of $b = 1.5$ for particle pair separation in fully developed turbulence [72–76].

7 Conclusions and prospects

In this thesis the dynamics of the granular Rayleigh-Taylor is studied in a rectangular Hele-Shaw cell. The affect of the interstitial fluid properties on the mixing of the grains is studied in experiments and well matched simulations. The numerical model was modified to account for fluid compressibility fluid inertia and viscous forces which lead to a hydrodynamic particle-particle coupling and a coupling between the fluid flow and the confining plates. In addition the model also includes solid friction between the particles and the plates. To verify the numerical model and its simplifications it was compared to well matched experiments. This test showed excellent agreement between the numerical model and the experiments. In regard of the mixing the compressibility of the interstitial fluid affects the dynamical patterns and the particle mixing much less than the viscosity. Depending on the viscosity the initial dynamics could be classified into two regimes. For low viscosities a ballistic particle pair separation was measured and for high fluid viscosity turbulent-dispersive particle pair separation was observed.
In a further work it will be of interest to study the dependency on system parameters of this transition from the ballistic to the turbulent-dispersive behavior.

8 Summary of the papers

In this thesis the effect of the interstitial fluid on the granular Rayleigh-Taylor instability is studied.

8.1 Paper 1

In the first paper a system with 140 μm sized grains and air or a water/glycerol solution as the interstitial fluid is studied and analyzed. Air provides an example of a compressible fluid while water/glycerol is a case of a fully incompressible fluid. Experiments are compared to well matched numerical simulations. A numerical hybrid model is developed that shows excellent agreement to the experiments. The resulting dynamics are analyzed by the means of velocity field histograms, Fourier transformations and 2 dimensional autocorrelation functions. The velocity field of the particles in the experiments is determined by a correlation image velocimetry technique in real space and improved by a filtering algorithm in real space.

8.2 Paper 2

The second paper adresses the question of what is causing the observed differences between a high viscous and incompressible fluid like water/glycerol, and a compressible low viscous fluid as i.e. air. In this paper it is shown that the compressibility of the air does not cause a significant difference of the dynamics of the particles for the systems sizes studied. However, the viscosity is shown to strongly affect the formation of the fingers causing the observed differences of the sedimentation in paper 1.

Bibliography

[1] Reisinger A. Duran, J. *Sands, Powders, and Grains: An Introduction to the Physics of Granular Materials.* Springer-Verlag New York, Inc., New York, 1999.

[2] A. Daerr and Stéphane Douady. Two types of avalanche behaviour in granular media. *Nature*, 399:241–243, 1999.

[3] Gordon C. Jacoby, Patrick L. Williams, and Brendan M. Buckley. Tree ring correlation between prehistoric landslides and abrupt tectonic events in seattle, washington. *Science*, 258(5088):1621–1623, 1992.

[4] P. Richard. Slow relaxation and compaction of granular systems. *Nature Materials 4*, pages 121–128, 2005.

[5] Otten L. Fayed, M.E. *Handbook of powder science & technology*. Springer-Verlag, 1997.

[6] C. A. Coulomb. Essay on the rules of maximis and minimis applied to some problems of equilibrium related to architecture. *Acad. R. Mem. Phys. Divers Savants*, 7:343, 1773.

[7] M. Faraday. On a peculiar class of acoustical figures. *Trans. R. Soc. Lond.*, 121:299–340, 1831.

[8] O. Reynolds. On the dilatancy of media composed of rigid particles in contact. *Philos. Mag.*, 20:469–481, 1885.

[9] http://homeboyski.com/2008/01/31/what-you-need-to-know-about-avalanches-part-24-how-to-avoid-an-avalanche/.

[10] http://science.howstuffworks.com/quicksand-sinking.htm.

[11] http://geo.dpri.kyoto-u.ac.jp/division-e.html.

[12] http://seismo.berkeley.edu/blogs/seismoblog.php/2008/09/24/when-the-ground-gives-way.

[13] http://www.wdr.de/themen/wissen/umwelt/klimawandel/aktuelles/dossier.jhtml?pbild=1.

[14] Juliet F. Bird, Julian J. Bommer, Helen Crowley, and Rui Pinho. Modelling liquefaction-induced building damage in earthquake loss estimation. *Soil Dynamics and Earthquake Engineering*, 26(1):15 – 30, 2006.

[15] Eiichi Kuribayashi and Fumio Tatsuoka. Brief review of liquefaction during earthquakes in japan. *Soils and Foundations*, 15(4):81–92, 19751215.

[16] J. F. Peters, M. Muthuswamy, J. Wibowo, and A. Tordesillas. Characterization of force chains in granular material. *Phys. Rev. E*, 72(4):041307, 2005.

[17] M. E. Cates, J. P. Wittmer, J.-P. Bouchaud, and P. Claudin. Jamming, force chains, and fragile matter. *Phys. Rev. Lett.*, 81(9):1841–1844, 1998.

[18] T. S. Majmudar and R. P. Behringer. Contact force measurements and stress-induced anisotropy in granular materials. *Nature*, 435:1079–1082, 2005.

[19] H.A. Janssen. Versuche über getreidedruck in silozellen. *Zeitschrift des Vereines Deutscher Ingenieure*, 39:1045–1049, 1892.

[20] E. Clément, J. Duran, and J. Rajchenbach. Experimental study of heaping in a two-dimensional ‘‘sand pile’’. *Phys. Rev. Lett.*, 69(8):1189–1192, 1992.

[21] Sidney R. Nagel. Instabilities in a sandpile. *Rev. Mod. Phys.*, 64(1):321–325, 1992.

[22] J. A. C. Gallas, H. J. Herrmann, and S. Sokołowski. Convection cells in vibrating granular media. *Phys. Rev. Lett.*, 69(9):1371–1374, 1992.

[23] A. P. J. Breu, H.-M. Ensner, C. A. Kruelle, and I. Rehberg. Reversing the brazil-nut effect: Competition between percolation and condensation. *Phys. Rev. Lett.*, 90(1):014302, 2003.

[24] J. Duran, T. Mazozi, E. Clément, and J. Rajchenbach. Size segregation in a two-dimensional sandpile: Convection and arching effects. *Phys. Rev. E*, 50(6):5138–5141, 1994.

[25] Pierre Cizeau, Hernán A. Makse, and H. Eugene Stanley. Mechanisms of granular spontaneous stratification and segregation in two-dimensional silos. *Phys. Rev. E*, 59(4):4408–4421, 1999.

[26] Hernán A. Makse, Pierre Cizeau, and H. Eugene Stanley. Possible stratification mechanism in granular mixtures. *Phys. Rev. Lett.*, 78(17):3298–3301, 1997.

[27] Xiang Cheng, German Varas, Daniel Citron, Heinrich M. Jaeger, and Sidney R. Nagel. Collective behavior in a granular jet: Emergence of a liquid with zero surface-tension. *Phys. Rev. Lett.*, 99:188001, 2007.

[28] John R. Royer, Eric I. Corwin, Bryan Conyers, Andrew Flior, Mark L. Rivers, Peter J. Eng, and Heinrich M. Jaeger. Birth and growth of a granular jet. *Physical Review E (Statistical, Nonlinear, and Soft Matter Physics)*, 78(1):011305, 2008.

[29] John R. Royer, Daniel J. Evans, Loreto Oyarte, Eliot Kapit Qiti Guo, Matthias E. Möbius, Scott R. Waitukaitis, and Heinrich M. Jaeger. High-speed tracking of rupture and clustering in freely falling granular streams. *Nature*, 459:1110, 2009.

[30] A. Betat, V. Frette, and I. Rehberg. Sand ripples induced by water shear flow in an annular channel. *Phys. Rev. Lett.*, 83(1):88–91, 1999.

[31] Hiraku Nishimori and Noriyuki Ouchi. Formation of ripple patterns and dunes by wind-blown sand. *Phys. Rev. Lett.*, 71(1):197–200, 1993.

[32] Alexandre Stegner and José Eduardo Wesfreid. Dynamical evolution of sand ripples under water. *Phys. Rev. E*, 60(4):R3487–R3490, 1999.

[33] E Somfai, A Czirok, and T Vicsek. Power-law distribution of landslides in an experiment on the erosion of a granular pile. *Journal of Physics A: Mathematical and General*, 27(20):L757–L763, 1994.

[34] M. A. Hampton, H. J. Lee, and J. Locat. Submarine landslides. *Rev. Geophys.*, 34(1):33–59, 1996.

[35] A. Khaldoun, G. Wegdam, E. Eiser, and D. Bonn. Quicksand! *Europhysics News*, 37(4):18–19, 2006.

[36] A. Khaldoun, E. Eiser, G. H. Wegdam, and Daniel Bonn. Rheology: Liquefaction of quicksand under stress. *Nature*, 437:635, 2005.

[37] Ø. Johnsen, C. Chevalier, A. Lindner, R. Toussaint, E. Clement, K. J. Måløy, E. G. Flekkøy, and J. Schmittbuhl. Decompaction and fluidization of a saturated and confined granular medium by injection of a viscous liquid or gas. *Physical Review E (Statistical, Nonlinear, and Soft Matter Physics)*, 78(5):051302, 2008.

[38] Ø. Johnsen, R. Toussaint, K. J. Måløy, E. G. Flekkøy, and J. Schmittbuhl. Coupled air/granular flow in a linear hele-shaw cell. *Physical Review E (Statistical, Nonlinear, and Soft Matter Physics)*, 77(1):011301, 2008.

[39] Ø. Johnsen, R. Toussaint, K. J. Måløy, and E. G. Flekkøy. Pattern formation during air injection into granular materials confined in a circular hele-shaw cell. *Physical Review E (Statistical, Nonlinear, and Soft Matter Physics)*, 74(1):011301, 2006.

[40] http://research.yale.edu/jamming/?q=jammed_image.

[41] C. Bizon, M. D. Shattuck, J. B. Swift, W. D. McCormick, and Harry L. Swinney. Patterns in 3d vertically oscillated granular layers: Simulation and experiment. *Phys. Rev. Lett.*, 80(1):57–60, 1998.

[42] Farhang Radjai, Michel Jean, Jean-Jacques Moreau, and Stéphane Roux. Force distributions in dense two-dimensional granular systems. *Phys. Rev. Lett.*, 77(2):274–277, 1996.

[43] MOREAU J. J. Some numerical methods in multibody dynamics: application to granular materials. *Eur. J. Mech. A. Solids*, 13:93–114, 1994.

[44] Mario Nicodemi, Antonio Coniglio, and Hans J. Herrmann. Frustration and slow dynamics of granular packings. *Phys. Rev. E*, 55(4):3962–3969, 1997.

[45] Anthony Rosato, Katherine J. Strandburg, Friedrich Prinz, and Robert H. Swendsen. Why the brazil nuts are on top: Size segregation of particulate matter by shaking. *Phys. Rev. Lett.*, 58(10):1038–1040, 1987.

[46] O. Zik, Dov Levine, S. G. Lipson, S. Shtrikman, and J. Stavans. Rotationally induced segregation of granular materials. *Phys. Rev. Lett.*, 73:644–647, 1994.

[47] Eirik G. Flekkøy, Rafael Delgado-Buscalioni, and Peter V. Coveney. Flux boundary conditions in particle simulations. *Phys. Rev. E*, 72(2):026703, 2005.

[48] Lord Rayleigh. Investigation of the character of the equilibrium of an incompressible heavy fluid of variable density. *Proceedings of the London Mathematical Society*, 14:170–177, 1883.

[49] U. Alon, J. Hecht, D. Ofer, and D. Shvarts. Power laws and similarity of rayleigh-taylor and richtmyer-meshkov mixing fronts at all density ratios. *Phys. Rev. Lett.*, 74(4):534–537, Jan 1995.

[50] http://www.astro.virginia.edu/vita/athena/rt.html.

[51] M. Versluis, B. Schmitz, von der Heydt, A., and D. Lohse. How snapping shrimp snap: Through cavitating bubbles. *Science*, 289:2114–2117, 2000.

[52] Hao Lin, Brian D. Storey, and Andrew J. Szeri. Rayleigh–taylor instability of violently collapsing bubbles. *Physics of Fluids*, 14(8):2925–2928, 2002.

[53] W.H. Calvin. The great climate flip-flop. *The Atlantic Monthly*, 281:47–64, 1998.

[54] G. Bateman. *MHD Instabilities.* MIT Press, 1979.

[55] R.D. Petrasso. Rayleigh's challenge endures. *nature*, 367:217–218, 1994.

[56] A. Burrows. Supernova explosions in the universe. *nature*, 403:727–733, 2000.

[57] W. Schmidt. From tea kettles to exploding stars. *nature physics*, 2:505–506, 2006.

[58] M. Zingale, S.E. Woosley, C.A. Rendleman, M.S. Day, and J.B. Bell. Three-dimensional numerical simulations of rayleightaylor unstable flames in type ia supernovae. *Astrophysical Journal*, 632:1021–1034, 2005.

[59] A.Lange, M.Schröter, M.A.Scherer, A.Engel, and I.Rehberg. Fingering instability in a water-sand mixture. *Eur. Phys. J. B.*, 4:475–484, 1998.

[60] M.Schröter C.Völtz, G.Iori, A.Betat, A.Lange, A.Engel, and I.Rehberg. Finger-like patterns in sedimenting water sand suspensions. *Phys. Rep.*, 337:117–138, 2000.

[61] C. Völtz, W. Pesch, and I. Rehberg. Rayleigh-taylor instability in a sedimenting suspension. *Phys. Rev. E*, 65:011404, 2001.

[62] J. L. Vinningland, Ø. Johnsen, E. G. Flekkøy, R. Toussaint, and K. J. Måløy. Experiments and simulations of a gravitational granular flow instability. *Phys. Rev. E*, 76:051306, 2007.

[63] Jan Ludvig Vinningland, Øistein Johnsen, Eirik G. Flekkøy, Renaud Toussaint, and Knut Jørgen Måløy. Granular rayleigh-taylor instability: Experiments and simulations. *Physical Review Letters*, 99(4):048001, 2007.

[64] C. Völtz. Granular dynamics of density profiles in a suspension interface. *Phys. Rev. E*, 68(2):021408, Aug 2003.

[65] Stéphane Roux, François Hild, and Yves Berthaud. Correlation image velocimetry: A spectral approach. *Appl. Opt.*, 41:108–115, 2002.

[66] A. Lagarde. *Advanced optical methods and applications in solid mechanics*. Kluwer,Dordrecht (The Netherlands), 2000.

[67] Dragos-Victor Anghel, Martin Strauss, Eirik G. Flekkøy, Sean McNamara, and Knut Jørgen Måløy. Erratum: Structure formation and instability in a tube of sand [phys. rev. lett. [bold 87], 134302 (2001)]. *Physical Review Letters*, 97(5):059902, 2006.

[68] Dragos-Victor Anghel, Martin Strauss, Sean McNamara, Eirik G. Flekkoy, and Knut Jorgen Maloy. Erratum: Grains and gas flow: Molecular dynamics with hydrodynamic interactions [phys. rev. e [bold 61], 4054 (2000)]. *Physical Review E (Statistical, Nonlinear, and Soft Matter Physics)*, 74(2):029906, 2006.

[69] Sean McNamara, Eirik G. Flekkøy, and Knut Jørgen Måløy. Grains and gas flow: Molecular dynamics with hydrodynamic interactions. *Phys. Rev. E*, 61(4):4054–4059, Apr 2000.

[70] P.C. Carman. Fluid flow through a granular bed. *Trans. Inst. Chem. Eng.*, 15:150–156, 1937.

[71] et al William H Press. *Numerical recipes : the art of scientific computing*. Cambridge University Press, 2007.

[72] L. F. Richardson. Atmospheric diffusion on a distance-neighbour graph. *Proc. R. Soc. A*, 110:709, 1926.

[73] T. H. Dupree. A perturbation theory for strong plasma turbulence. *Physics Fluids*, 9:1773, 1966.

[74] T. H. Dupree. Theory of phase space density granulation in plasma. *Physics Fluids*, 15:334, 1972.

[75] G. Boffetta, A. Celani, A. Crisanti, and A. Vulpiani. Relative dispersion in fully developed turbulence: Lagrangian statistics in synthetic flows. *Europhys. Lett*, 46:177, 1999.

[76] R. Balescu J. H. Misguich. On relative spatial diffusion in plasma and fluid turbulences: Clumps, richardson law and intrinsic stochasticity. *Plasma Physics*, 24:289, 1982.